Nanoscale

PAPER

View Article Online
View Journal | View Issue

Cite this: *Nanoscale*, 2024, **16**, 8401

Enhanced photoelectrochemical water splitting using carbon cloth functionalized with ZnO nanostructures *via* polydopamine assisted electroless deposition†

Ian P. Seetoh, [a] Akhil K. Ramesh, [a] Wei Xin Tan[b] and Chang Quan Lai *[b,c,d]

ZnO nanorods (ZnO-nr) have been widely studied as a promising nanomaterial for photoelectrochemical water splitting. However, almost all prior studies employed planar electrodes. Here, we investigated the performance of ZnO nanorods on a fibrous carbon cloth (CC) electrode, which offers a larger surface area for functionalization of photocatalysts. ZnO nanorods and Ni nanofilm were deposited on carbon cloth substrates for investigation as the photoanode and cathode of a photoelectrochemical water splitting setup, respectively. The use of polydopamine in the electroless deposition of ZnO ensured a uniform distribution of nanorods that were strongly adherent to the microfiber surface of the carbon cloth. Compared to ZnO nanorods grown on planar ITO/glass substrates, the CC-based ZnO photoanodes exhibited smaller onset potentials (1.1 V_{RHE} *vs.* 1.8 V_{RHE}), ~40× larger dark faradaic currents at 1.23 V_{RHE} and 5.5×–9× improvement in photoconversion efficiencies. Ni/CC cathodes were also found to exhibit a lower overpotential@10 mA cm^{-2} than Ni/Cu by 90 mV. The photocurrent obtained from the ZnO-nr/CC anode was highly stable across an hour and the peak current decreased by only 5% across 5 cycles of illumination, compared to 72% for the planar ZnO-nr/ITO anode. However, the response of the CC-based setups to changes in the illumination conditions was slower, taking hundreds of seconds to reach peak photocurrent, compared to tens of seconds for the planar electrodes. Using cyclic voltammetry, the double-layer capacitance of the electrodes was measured, and it was shown that the increased efficiency of the ZnO-nr/CC anode was due to a 2 order of magnitude increase in electrochemically active sites provided by the copious microfiber surface of the carbon cloth.

Received 23rd February 2024,
Accepted 26th March 2024

DOI: 10.1039/d4nr00761a

rsc.li/nanoscale

1. Introduction

To avert the worst effects of global warming, it is imperative that the world decarbonizes its activities by transitioning to carbon-free energy sources. One possible way to achieve this is to make use of renewable energy for the electrolysis of water, so that the energy can be stored as green hydrogen without carbon emissions. As a fuel, hydrogen is appealing as it has a high energy content per unit weight and produces only H_2O upon combustion.

Electrolysis of water can be described by

$$H_2O(l) \rightarrow H_2(g) + \frac{1}{2}O_2(g), \quad E_0 = 1.23\ V \qquad (1)$$

where E_0 refers to the standard potential. This reaction consists of two half reactions – the hydrogen evolution reaction (HER) and the oxygen evolution reaction (OER),

$$HER\ (cathode):\ 4H^+ + 4e^- \rightarrow 2H_2, \quad E_0 = 0\ V \qquad (2)$$

$$OER\ (anode):\ 2H_2O \rightarrow O_2 + 4H^+ + 4e^-, \quad E_0 = 1.23\ V. \qquad (3)$$

The kinetics generally tend to be more sluggish with the OER, which takes place *via* a multi-step four-electron transfer process at the anode,[1] resulting in significant overpotentials which lower the efficiency of actual water splitting operations. To counter this, expensive noble metals such as platinum, rubidium, and iridium, and their oxides are often used as catalysts in electrolysis setups. In addition, non-noble metals such

[a]*Temasek Laboratories, Nanyang Technological University, 50 Nanyang Drive, Singapore 637553, Singapore*
[b]*School of Materials Science & Engineering, Nanyang Technological University, 50 Nanyang Ave, Singapore 639798, Singapore. E-mail: cqlai@ntu.edu.sg*
[c]*School of Mechanical & Aerospace Engineering, Nanyang Technological University, 50 Nanyang Ave, Singapore 639798, Singapore*
[d]*Singapore Centre for 3D Printing, Nanyang Technological University, 63 Nanyang Drive, Singapore 636922, Singapore*

†Electronic supplementary information (ESI) available: (S1) Details of *iR*-compensation and (S2) ZnO nanorod growth on carbon cloth without polydopamine or seeding. See DOI: https://doi.org/10.1039/d4nr00761a

as nickel, together with its alloys and compounds, are also being actively investigated as alternative catalysts to reduce material costs.[2,3]

Another way to address high overpotentials in the OER is to make use of photosensitive catalysts to partially or fully provide the electrical energy required for water splitting.[4–7] Such photoelectrochemical (PEC) cells can enable significant water splitting to proceed at potential differences *below* 1.23 V, significantly reducing power consumption. Compared to the use of separate solar harvesting and electrolysis modules, the PEC cell also presents itself as an attractive 2-in-1 integrated solution that can potentially be simpler and more cost-effective to implement.

Amongst the photocatalysts investigated for solar PEC cells, ZnO is one of the most widely studied materials.[4–11] It is a non-toxic and low-cost II–VI semiconductor with a large direct bandgap of 3.26 eV,[12] high carrier mobility[13] and tendency to form nanostructures of high crystalline quality.[11,14,15] Its valence band edge is also favourably aligned against the oxidation potential of water to facilitate the photo-catalysis of the OER.[16,17] However, the photoconversion efficiency of ZnO is relatively low, since it absorbs light primarily in the UV region and it has limited intrinsic catalytic activity towards the oxidation of water.

To circumvent these constraints, we propose depositing ZnO on carbon cloth (CC) for the fabrication of the photoanode. Compared to the usual planar ITO/glass or FTO-based substrates, the fibrous carbon cloth can offer a larger surface area for the growth of more ZnO nanorods, greatly increasing the catalytically active sites for PEC water splitting. CC also exhibits good electrical conductivity and chemical stability, which are necessary properties for an anode. For these reasons, carbon cloth has been increasingly investigated as a catalyst support for water splitting experiments in recent years with promising results.[18–22] Its popularity, however, has yet to propagate to investigations involving PEC cells, which is a key reason CC was selected for investigation here.

For the present investigation, ZnO nanorods were synthesized on carbon cloth *via* a polydopamine-assisted electroless deposition technique, which is a highly scalable process that is more suitable for coating non-planar substrates like carbon cloth than the conventional spin-coating sol–gel method.[11] The functionalized carbon cloth was then studied as a photoanode for the OER under near-neutral pH conditions. Subsequently, the photoanode was paired with a Ni-coated carbon cloth cathode, which enabled the HER, to form a complete PEC cell for further investigations, including 2-electrode efficiency measurements which are rarely reported in ZnO photoelectrochemical experiments elsewhere. ZnO nanorods grown on a planar ITO coated glass substrate acted as the control, against which the carbon cloth photoanode was primarily assessed for the effect of *planar vs. fibrous* substrates. We also studied how the effects of polydopamine and the microstructure of ZnO affect the photoelectrochemical properties.

Chang Quan Lai

Changquan Lai received his PhD degree from the National University of Singapore in Advanced Materials for Micro- and Nano-Systems, with support from the Singapore-MIT Alliance Fellowship. He carried out his postdoctoral studies in Singapore, ETH Zurich and Caltech under the auspices of the SMART Fellowship and Temasek Research Fellowship. He was awarded the START scholarship in 2021 and is currently a Nanyang Assistant Professor in Nanyang Technological University. A key focus of his recent research lies on upcycling of waste products into nanomaterials for green technologies, which has received attention from mainstream media, including the World Economic Forum.

2. Materials and methods

2.1. Material synthesis

Carbon cloth (CC) was fabricated through the pyrolysis of 100% cotton textile in a tube furnace under an argon atmosphere. The textile sample was heated at a rate of 5 °C min^{-1} from room temperature to a peak temperature of 800 °C and held for 1 h. Prior to functionalization with Ni and ZnO, the CC substrates were cleaned by sonicating in isopropyl alcohol and then in deionized water. For the cathode, the samples were coated with nickel using electroless deposition (ELD). The substrate (CC or copper foil) was first activated using a conventional two-step Sn + Pd procedure, where the sample was immersed in $SnCl_2$ (2 mg mL^{-1}) + HCl (20 mL L^{-1}) for 5 min, followed by a solution containing $PdCl_2$ (0.2 mg mL^{-1}) + HCl (20 mL L^{-1}) for 10 min. The sample was then immersed in an aqueous electroless deposition bath containing 0.22 M lactic acid, 0.027 M diammonium citrate, 0.06 M $NiSO_4$, and 0.034 M dimethylamine borane (DMAB), for 1 h at 30 °C and pH 6.5 (adjusted by adding NaOH). After that, the samples were rinsed thoroughly with deionized water and dried in an oven at 60 °C for 15 min.

For the photoanode, the substrates (CC or indium tin oxide (ITO)-on-glass) were first coated with polydopamine for 24 h by immersing them in an aqueous solution containing 2 mg mL^{-1} dopamine HCl and 0.01 M Tris-HCl (pH adjusted to 8.5 by adding NaOH). The samples were then rinsed thoroughly with deionized water and placed in a solution containing $PdCl_2$ (0.2 mg mL^{-1}) + HCl (20 mL L^{-1}) for 10 min. After that, a ZnO seed layer was deposited on the Pd-activated substrate by electroless deposition in an aqueous bath containing 0.05 M $Zn(NO_3)_2$ and 0.05 M DMAB at 75 °C for 30 min. The seeded samples were then subjected to hydrothermal growth of ZnO

nanorods at 95 °C for 16 h in a sealed PTFE jar containing 0.05 M $Zn(NO_3)_2$ and 0.05 M hexamethylenetetramine (HMTA). At the end of growth, the samples were rinsed thoroughly with deionized water and dried in an oven at 60 °C for 15 min. To investigate the effect of the polydopamine coating on ZnO growth, another set of CC and ITO-on-glass samples were subjected to the same procedure but without the polydopamine coating and with the same two-step Sn + Pd treatment as described earlier (for ELD nickel),[23,24] before the electroless deposition of the ZnO seed layer.

2.2. Material characterization

Field-emission scanning electron microscopy was performed using a JEOL JSM-7600F machine that was coupled with a detector for energy dispersive X-ray (EDX) spectroscopy. X-ray photoelectron spectroscopy (XPS) spectra were recorded over an elliptical area of 700 × 300 μm^2 using a Kratos AXIS Supra (Al Kα source, 225 W) for surface analysis. UV photoelectron spectroscopy (UPS) was also performed using the same system with a He(I) monochromatic light source. Structural characterisation to investigate the crystalline nature of the samples was performed using X-ray diffraction (XRD, Bruker D8 Advance) with CuKα radiation. The measurements were carried out in a Bragg–Brentano geometry ($\theta/2\theta$ scan) and the scan range used was 10–80° with a scan speed of 0.05° s^{-1} to obtain the intensity *vs.* 2θ plot.

Optical absorbance and reflectance spectroscopy was performed using a Lambda 950 UV-Vis-NIR spectrophotometer. The light source was a tungsten halogen and/or a deuterium UV lamp and the spectra were obtained with an optical wavelength resolution of 1 nm. Fourier-transform infrared (FTIR) spectroscopy was performed using a Frontier PerkinElmer machine that uses a universal attenuated total reflectance (ATR) attachment to obtain spectra at a resolution of 0.1 cm^{-1}. Raman spectroscopy was performed using a WITec Alpha300 SR system with a 488 nm laser.

2.3. Electrochemical characterization

The Ni- (cathode) and ZnO-coated (photoanode) samples were used as working electrodes for electrochemical water splitting in a 3-electrode configuration using a potentiostat (Ossila T2006B1-UK). Ag/AgCl (3 M NaCl) and platinum wire were used as the reference and counter electrodes, respectively. The measured potentials ($E_{Ag/AgCl}$) were converted to reference hydrogen potentials (E_{RHE}) *via*

$$E_{RHE} = E_{Ag/AgCl} + 0.21 + 0.059pH \quad (4)$$

The electrolyte was 0.5 M Na_2SO_4 (pH ~ 7.5). The choice of a near-neutral pH electrolyte here has practical significance. Most reported electrochemical water splitting studies utilized highly alkaline (pH ~ 14) or acidic (pH ~ 1) electrolytes[25,26] since reaction rates with neutral pH electrolytes are generally slower in comparison.[27] However, water splitting at near-neutral pH can enable the direct electrolysis of seawater with minimal pretreatment or without desalination.[27–30] The process is more sustainable as it is expected to experience fewer problems with corrosion of electrolysis equipment after long-term use, along with further benefits of safer and more environmentally friendly working conditions.

Linear sweep voltammetry (LSV) was performed at a scan rate of 5 mV s^{-1}. Chronoamperometry (CA) was performed at selected voltages for Tafel slope calculations and photoresponse studies. Cyclic voltammetry (CV) was conducted at different scan rates from 5 to 50 mV s^{-1} to estimate the electrochemical double layer capacitance (C_{dl}), which is a representation of the effective electrochemical surface area (ECSA). Additional CV measurements were also performed at a fast scan rate of 100 mV s^{-1} over 1 h to assess the stability of the electrode. The measured currents were presented as current densities (in mA cm^{-2}) by normalizing against the geometric area of the sample (~0.25 cm^2). Selected data were *iR*-compensated during post-processing using the 'current interrupt' method[31,32] by using an oscilloscope (MDO 3014, Tektronix) connected to the working and reference electrodes of the electrochemical cell (see ESI S1†). The photoelectrochemical properties were studied by exposing the ZnO photoanode to simulated sunlight (30 mW cm^{-2}) from an 80 W xenon lamp with an attached AM1.5 filter. Selected samples from 3-electrode measurements were subsequently paired together and studied in a 2-electrode configuration.

3. Results

3.1. Material synthesis and characterization

3.1.1. ZnO nanorods/carbon cloth photoanode. SEM images of the carbon cloth (CC) are shown in Fig. 1A at various magnifications. It can be observed that the carbon cloth retained the fabric morphology of woven microfibers, which had diameters in the range of 1–10 μm. This result is consistent with the pyrolysis of cloth[19] and even paper,[33] which does not alter the microstructural morphology of the material significantly, beyond shrinking the cellulose fibers.

Fig. 1B shows the carbon cloth functionalized with ZnO nanorods (ZnO-nr). ZnO-nr growth usually requires the deposition of a precursor seed layer composed of densely packed ZnO nanoparticles. In previous studies, the ZnO seed layer was often formed by spin-coating and annealing a sol–gel at high temperature (up to 500 °C).[11] While spin-coating is a simple and effective method for depositing sol–gel evenly on planar substrates, such as FTO- or ITO-on-glass, it cannot coat porous substrates, like CC, well.

For this reason, we have opted to generate the seed layer using polydopamine-assisted electroless deposition, which proceeds *via* a 3-step procedure – (1) coating of the carbon cloth with polydopamine, (2) electroless deposition of a ZnO seed layer, and (3) hydrothermal growth of ZnO nanorods. This procedure was also applied to synthesize ZnO-nr on ITO coated glass, a common substrate used in previous photoelectrochemical studies,[4–6,8–10,34] to produce planar control

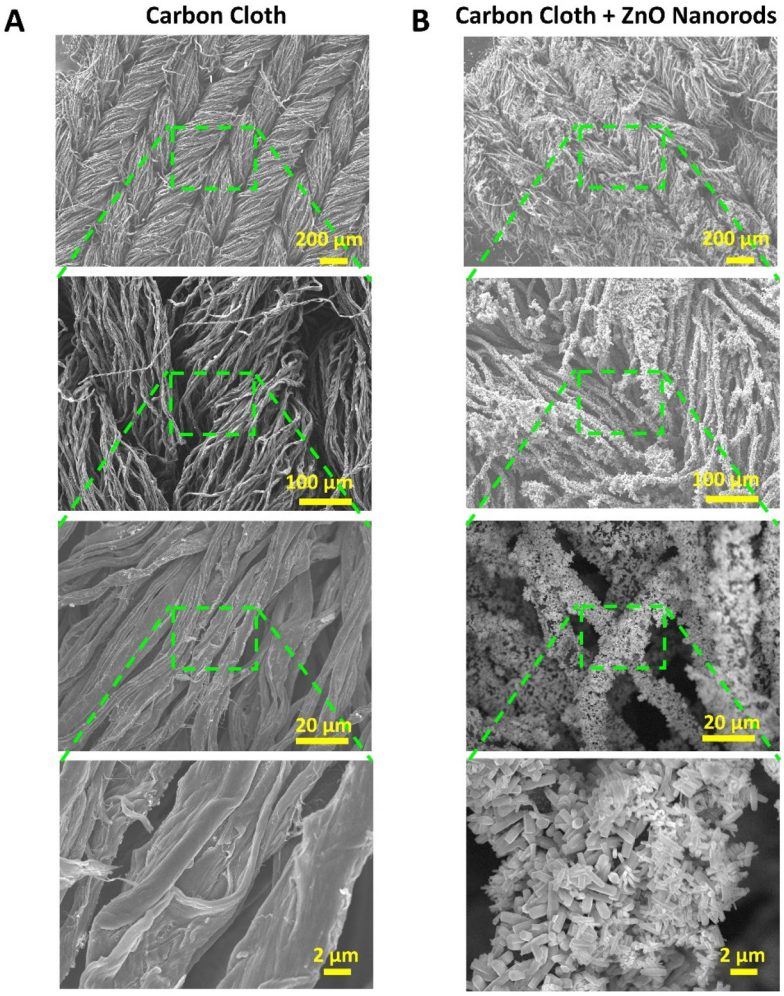

Fig. 1 SEM images at increasing magnification from top to bottom, showing the structures of (A) carbon cloth and (B) carbon cloth functionalized with ZnO nanorods.

samples. SEM images of the CC and ITO samples after each fabrication step are shown in Fig. 2A and B.

The polydopamine coating in step (1) was formed through a bioinspired process that begins with the oxidation and subsequent self-polymerization of dopamine molecules.[35] This results in a thin polymeric nanofilm that coats onto all kinds of surfaces[35] and is, itself, easily functionalized by other chemical species for a wide variety of applications.[36] The exact structure of the polydopamine coating remains uncertain, although many possibilities have been hypothesized.[36] Nevertheless, it is known that the dopamine precursor itself consists of a catechol group attached to the end of an ethyl amine chain (see the inset at the top-left corner of Fig. 2C). The nitrogen atoms from amine groups can be readily detected as N 1s using XPS, which then serves as an identifier for the presence of polydopamine on the substrates (Fig. 2C). Peak fitting of the high-resolution data from the N 1s signal revealed 3 peaks: (i) the main peak at 399.6 eV for R–NH_2 corresponding to primary amines from the dopamine precursor, (ii) R–NH–R at 401.7 eV corresponding to secondary amines related to species formed in the early stages of polymerization, and (iii) R═N–R at 397.6 eV related to imines or tertiary/aromatic amines formed in the later stages of polymerization.[37–42]

A key role of polydopamine here is to encourage the adsorption of Pd ions onto the substrate surface for the subsequent ZnO electroless deposition process. Pd ions were introduced by dipping the polydopamine-coated substrates into $PdCl_2$/HCl solution,[43–45] and can be detected with the Pd 3d signal in XPS, along with traces of chlorine, as indicated by the Cl 2s and Cl 2p peaks (Fig. 2C). Peak fitting of the high-resolution data from the Pd 3d signal reveals that the signal was primarily contributed by Pd^{2+} $3d_{3/2}$ (342.8 eV) and $3d_{5/2}$ (337.6 eV) peaks associated with $PdCl_2$,[46] in agreement with an earlier study on palladium functionalized polydopamine.[44] In addition, low energy shoulders were also found at 341.4 eV and 335.9 eV, which can be attributed to traces of non-ionized Pd^0 that might have formed by partial reduction of Pd^{2+} by catechol groups.[45] The adsorbed Pd was, in turn, essential for catalyzing the reduction of nitrate ions by DMAB[47,48] in the ZnO elec-

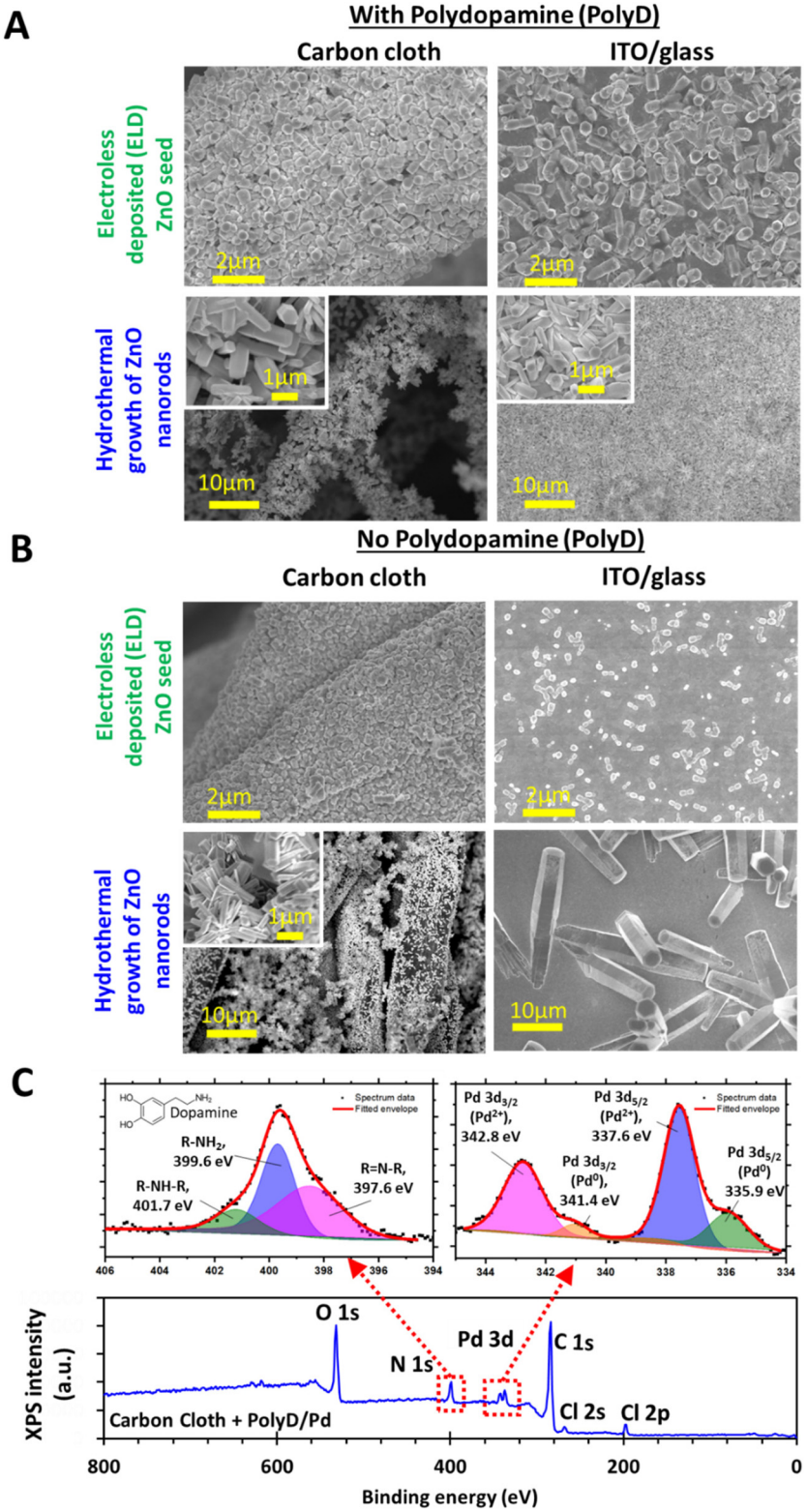

Fig. 2 (A) Comparison of ZnO grown on substrates (carbon cloth and ITO/glass) with polydopamine or (B) without polydopamine. Insets: higher magnification images of selected samples. (C) XPS spectrum of the surface of the polydopamine-coated carbon cloth that was immersed in $PdCl_2$/HCl solution, along with fitted high resolution data for N 1s and Pd 3d.

troless deposition process. According to Izaki and Omi,[23] this reduction then led to the formation of $Zn(OH)_2$, which was eventually dehydrated to form a dense layer of ZnO nanoparticles (*i.e.* seeds) on the polydopamine-coated microfibers of the carbon cloth, as well as the planar ITO surface (Fig. 2A).

Following this, ZnO nanorods were grown using a widely reported hydrothermal growth procedure involving zinc nitrate and HMTA,[14,49] where growth along the *c*-axis crystal direction of wurtzite ZnO was promoted at the expense of other directions. This resulted in a uniform distribution of randomly oriented nanorods (diameter < 500 nm, length ~ 2 μm), mostly with hexagonal cross-sections (Fig. 1B and 2A). Similar results were also obtained for the polydopamine-coated ITO/glass substrates (Fig. 2A).

For carbon cloth without polydopamine, the ZnO seed layer consisted of smaller grains than its polydopamine-coated counterpart (Fig. 2B). Consequently, the ZnO nanorods had slightly smaller diameters, but displayed a poorer distribution, with some regions on the microfibers exhibiting a distinctly lower concentration of nanorods. This result illuminates the second key role of polydopamine – enhancing the adhesion of the ZnO nanorods to the substrates after formation. The empty patches found on the microfibers were likely caused when ZnO nanorods fell away during the rinsing process after hydrothermal growth.

On the planar ITO/glass substrates, very little ZnO was seeded by electroless deposition without polydopamine, which caused the resulting ZnO nanorods to be few and coarse (Fig. 2B). It is likely that the Pd ions had difficulty adsorbing onto the ITO surface, in contrast to that on carbon or polydopamine. It is also worth noting that direct hydrothermal growth without polydopamine or the ZnO seed layer led to extremely poor growth results, with hardly any ZnO nanorods found (Fig. S2 in the ESI†).

The underlying chemistry of ZnO nanorod samples was further analyzed by Raman and FTIR spectroscopy (Fig. 3A and B). In Fig. 3A, Raman peaks corresponding to the main vibrational modes of ZnO were clearly detected, along with the D- and G-bands of carbon from the carbon cloth. FTIR spectroscopy conducted on ZnO-nr/ITO samples clearly showed a Zn–O peak at the right-side edge of the spectrum (~600 cm^{-1}), while traces of hydroxyl groups, probably related to the underlying polydopamine, were detected as a broad signal at around 3400 cm^{-1}. Note that the carbon cloth samples could not be assessed using FTIR due to carbon cloth's poor transmittance in the infrared spectrum.

The optical properties of ZnO/PolyD (*i.e.* polydopamine)/ITO samples are shown in Fig. 3C and D. The ITO/glass sample itself exhibited a sharp absorption band-edge at around 350 nm. When coated with polydopamine, which was of dark brown coloration, the sample absorbed more light in the visible region, evident from the gentle slope of the orange curve between 400 and 700 nm in Fig. 3C. After the formation of the ZnO nanorods, the absorption band-edge shifted towards the higher wavelengths (~400 nm) *i.e.* lower photon energies, which is expected, since the bandgap of ZnO (~3.26 eV) is smaller than that of ITO (~4 eV). Similar trends were observed with the reflectance measurements of the same samples.

XRD characterization of ZnO-nr/CC samples revealed diffraction peaks that correspond to the hexagonal wurtzite crystal structure of ZnO (Fig. 3E). The peaks are very sharp and well-resolved, suggesting that the nanorods were highly crystalline. This is confirmed by a sharp photoluminescence signal at 320 nm, which was obtained during optical reflectance measurements (Fig. 3D).

3.1.2. Ni nanofilm/carbon cloth cathode. To fabricate the cathode for the HER part of the water splitting process, Ni was also deposited onto carbon cloth (CC) by electroless deposition. Since the SEM images for Ni/CC and plain CC appear very similar, it can be inferred that the Ni coating was uniform and conformal with the microfiber surface (Fig. 1A and Fig. 4A). For this electroless deposition procedure, the conventional 2-step Sn + Pd surface treatment was sufficient to make Pd adsorb onto the carbon surface and catalyze the reduction of Ni^{2+} into Ni metal with DMAB.

The uniformity of the Ni coverage was confirmed with EDX mapping (Fig. 4B and C). Signals from the underlying carbon and surface oxide on Ni were also detectable, but they were significantly weaker than those from Ni, appearing only for the parts of the microfiber that were highly focused. The thickness of the Ni coat was ascertained to be ~770 nm for the fabrication parameters used in this study (Fig. 4D). XRD measurements (Fig. 4E) detected a Ni (111) peak, which is associated with the face-centred cubic crystalline structure commonly found in nickel. In addition, the (002) peak points to the presence of graphite nanocrystals in the carbon cloth, which is common for pyrolyzed cellulose.[33]

3.2. Electrochemical characterization

3.2.1. ZnO photoanode: effect of substrate type. Linear sweep voltammetry (LSV) curves of fibrous carbon cloth (CC) anodes (ZnO-nr/CC, CC only) and planar anodes (ZnO-nr/ITO) are shown in Fig. 5A and B. In the absence of photoexcitation (*i.e.* 'dark' setting), ZnO-nr/CC exhibited large current densities in the range of mA cm^{-2}, with a distinct faradaic slope. The faradaic onset occurred at ~1.1 V and was slightly smaller than 1.23 V, the standard potential for the OER. The electrochemical performance was further enhanced when the anode was illuminated with light, with improved current density being observed for 0.5 V and above. In comparison, the current densities from the LSV curves for planar ZnO-nr/ITO samples (Fig. 5A and B) appeared insignificant, even when the sample was illuminated. In the dark, ZnO /ITO exhibited negligible current density until the onset of the faradaic slope at ~1.8 V. When illuminated, small photocurrents in tens of μA cm^{-2} could be measured at a potential difference of less than 1.23 V. This is a distinct feature of photoanodes and agrees well with previous reports that studied ZnO on planar ITO or FTO substrates.[4–7]

The cyclic photo-responses of planar ITO and fibrous CC photoanodes are compared in Fig. 5C. The gray trend indicates

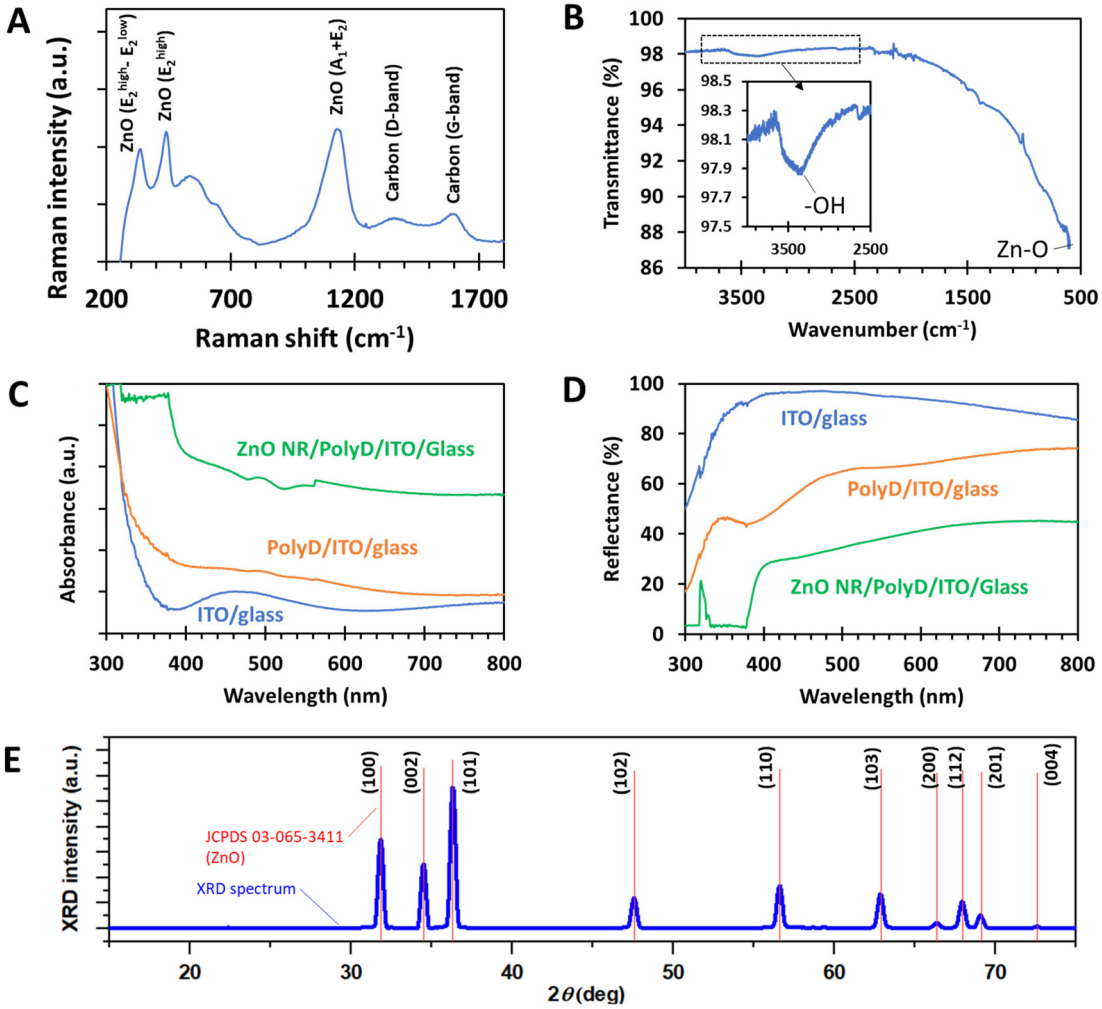

Fig. 3 (A) Raman spectroscopy spectrum of ZnO nanorods (ZnO-nr) on carbon cloth (CC). (B) FTIR spectroscopy spectrum of ZnO nanorods (ZnO-nr) on ITO/glass. (C) Optical absorbance and (D) reflectance of ZnO nanorods (ZnO-nr) on ITO/glass samples at various stages of material synthesis. (E) X-ray diffraction spectrum of ZnO nanorods on carbon cloth.

that CC, by itself, was insensitive to the presence of light. Comparing the bold orange and blue trends, it can be observed that the difference in current density for ITO- and CC-based ZnO samples was less than that suggested by Fig. 5A. This is likely because of the large surface area of the fibrous ZnO/CC, which led to large capacitive currents during LSV tests. Such currents, however, can be suppressed under steady-state chronoamperometry (CA) measurement,[50] leading to the discrepancy between Fig. 5A and C. Nevertheless, even in the absence of capacitive effects, the current density obtained from ZnO/CC in Fig. 5C was still significantly larger than that obtained from ZnO/ITO, ~40× and ~10× for dark and bright conditions, respectively. The large dark current of 0.23 mA cm^{-2} from ZnO/CC also suggests that the electrode can carry out a substantial OER even in the dark. This is probably due to the sheer amount of ZnO nanorods available for electrochemical reactions, which was made possible by the very large real surface area offered by CC.

Moreover, it was observed that the peak current density for the ZnO-nr/ITO sample decreased by 72% after 5 illumination cycles, compared with a decrease of 5% in the ZnO-nr/CC sample. This result indicates that the photo-response of ZnO-nr/CC was more stable. However, the photocurrents in the ZnO-nr/CC samples took longer to rise and fall in response to changes in the illumination – hundreds of seconds (ZnO-nr/CC) *vs.* tens of seconds (ZnO-nr/ITO). This is, again, due to the higher capacitance (*i.e.* higher RC time delay) of the CC-based sample, caused by the large surface area of the carbon microfibers.

Going further, the photoconversion efficiency η of the different photoanode substrates was also assessed using[16]

$$\eta = \frac{J'(1.23 - V)}{P_{in}}, \quad (5)$$

where J' refers to the current density at a given V, which refers to the potential relative to the open circuit voltage[4] and P_{in}

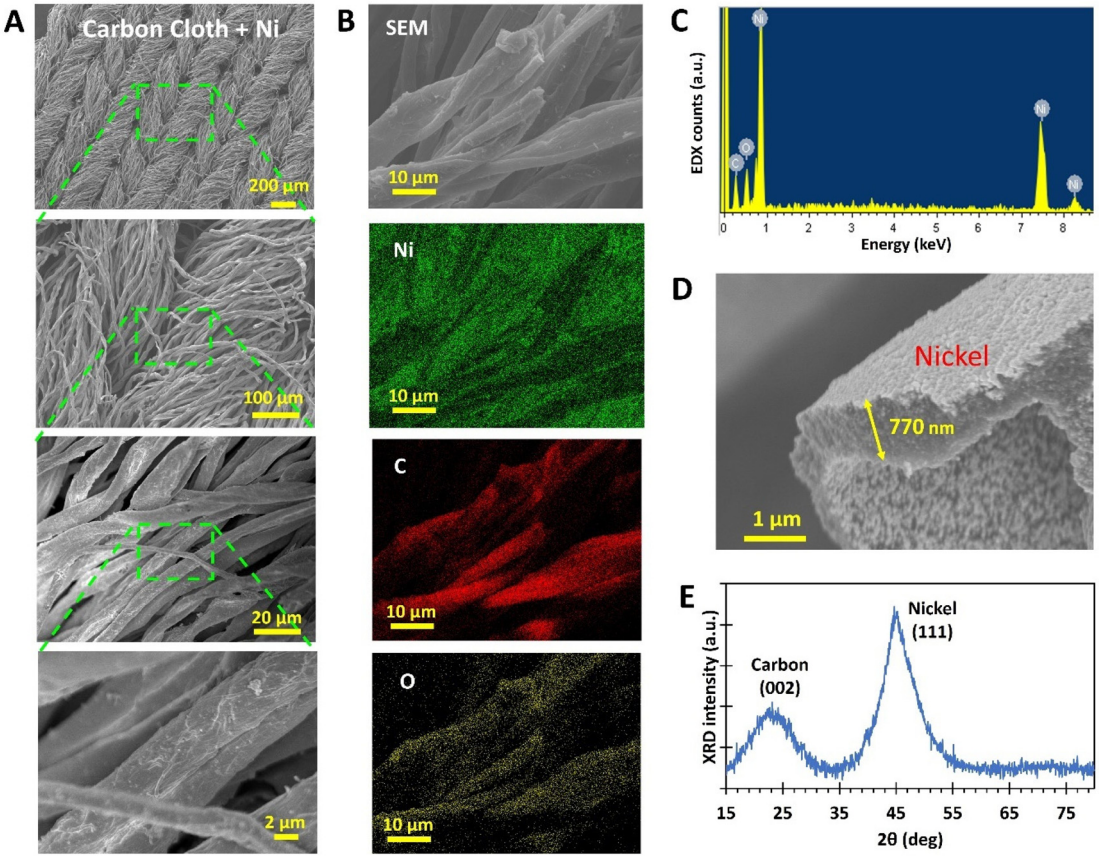

Fig. 4 (A) SEM images at increasing magnification from top to bottom, showing the microstructure of carbon cloth (CC) functionalized with a Ni coating. (B) SEM image of a Ni/CC sample along with EDX elemental mapping and the (C) corresponding EDX spectrum. (D) Image of a broken Ni coated carbon fiber, with the carbon core missing and only the Ni shell remaining. (E) XRD spectrum of a Ni/CC sample.

refers to the power density of illumination. For most cases in the literature,[4,5,8,34] J' is taken to be the LSV current density obtained under illumination, since the current density in the dark is usually negligible (Fig. 5B). However, for the ZnO-nr/CC samples (Fig. 5A) in this study, the dark current was substantial even at potentials below 1.23 V due to both strong capacitive effects and faradaic currents. Therefore, a more accurate computation of the photoconversion efficiency would be to take J' as the difference between the 'bright' and 'dark' currents.

As shown in Fig. 5D, maximum efficiencies of 0.45% and 0.05% were exhibited by ZnO-nr/CC and ZnO-nr/ITO, respectively *i.e.* the fibrous CC-based photoanode showed an efficiency that was 9× that of the planar ITO-based sample. ZnO nanostructures grown on planar substrates reported elsewhere[4,5,8,34] typically exhibit maximum photoconversion efficiencies in the range of 0.03% to 0.15%. In this regard, the efficiency of our ZnO planar electrode (*i.e.* ZnO-nr/ITO) is comparable to literature values, while the ZnO fibrous electrode (*i.e.* ZnO-nr/CC) outperforms many other ZnO photoanodes in the literature.

3.2.2. Effect of polydopamine and ZnO morphology on photoanodic current. Data from other control samples are also presented in Fig. 5C as thin curve lines for comparison. These include ZnO nanorods grown on carbon cloth without polydopamine (ZnO-nr/CC (no PolyD)), a ZnO seed layer on polydopamine on carbon cloth (ZnO-seed/CC) and a ZnO seed layer on carbon cloth without polydopamine (ZnO-seed/CC(no PolyD)). The data from ZnO seeds on ITO substrates are not shown as their current densities and photoresponse were barely noticeable. Comparing ZnO-seed/CC and ZnO-seed/CC (no PolyD) after 5 cycles of illumination, it can be observed that the presence of polydopamine slightly raised the photocurrent of ZnO by ~9%. Their similar performance reflects the growth results shown earlier in section 3.1.1, where good coverage of the seed layer can be achieved with and without polydopamine. On the other hand, ZnO-nr/CC exhibited a bright current that was about twice that of ZnO-nr/CC (no PolyD). These results are expected, since empty patches of missing ZnO material were observed with samples without polydopamine (Fig. 2A and B), clearly illustrating the importance of polydopamine as an adhesive for the firm attachment of ZnO nanorods on the carbon cloth fibers.

Next, by comparing ZnO-nr/CC with ZnO-seed/CC, it can be observed that the morphology of the nanorods significantly improved the photocurrent density by 172%. This result shows

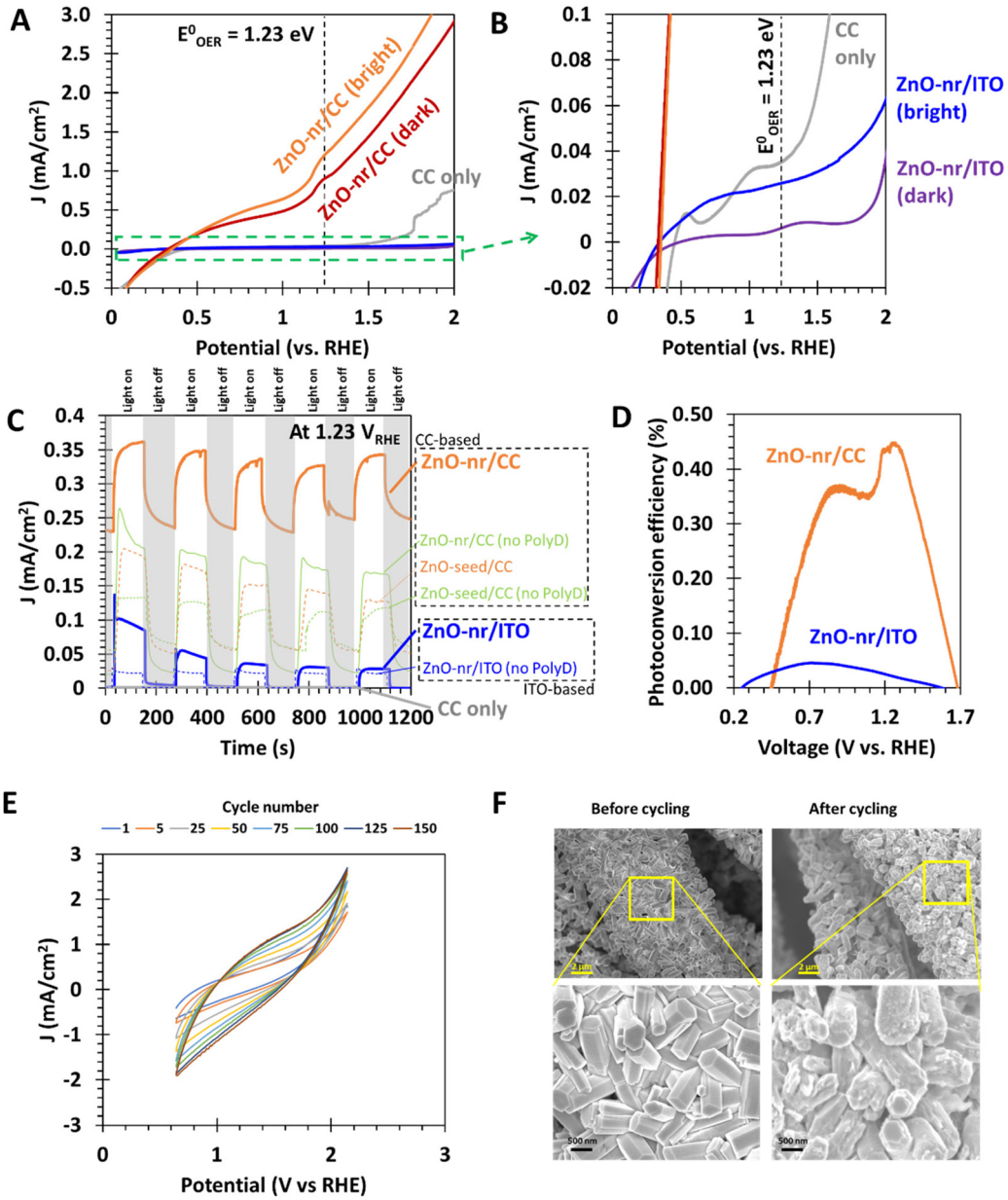

Fig. 5 Linear sweep voltammetry (LSV) curves of photoanodes composed of (A) ZnO nanorods on carbon cloth (ZnO-nr/CC) and (B) ZnO nanorods on planar ITO/glass (ZnO-nr/ITO). Dark – ambient; bright – AM1.5 simulated sunlight. Results from plain carbon cloth (CC only) under dark conditions are also shown as control. (C) Chronoamperometry (CA) at 1.23 V_{RHE} for ZnO-nr/CC, ZnO-nr/ITO and plain CC anodes in the presence and absence of photoexcitation. Also shown are data from samples without polydopamine (PolyD) and with only electroless deposited ZnO seeds. (D) Photoconversion efficiency of ZnO photoanodes. (E) Cyclic voltammetry at 0.1 V s^{-1} of ZnO-nr/CC over 150 cycles. (F) SEM images of ZnO-nr/CC comparing the surface morphology before and after 150 cycles of cyclic voltammetry.

that the enhanced surface area of nanorods is an effective promoter of the water splitting kinetics. The effect is similar, albeit less pronounced, in samples without polydopamine coating – ZnO-nr/CC (no PolyD) exhibited a photocurrent 44% higher than that of ZnO-seed/CC (no PolyD). This decrease in enhancement may have been caused by the nanorods falling off during rinsing of the samples after ZnO nanorod growth. Without the polydopamine adhesive, the coverage of the ZnO nanorods became less than that of the ZnO seed layer, which can be observed in Fig. 2B.

It was reported in several studies that OER rates tend to be faster on the polar (001) face of wurtzite ZnO nanorods, rather than on the non-polar (100) and (110) faces.[51,52] Given the hexagonal cross-section of the nanorods (Fig. 1B) and with reference to earlier studies using similar hydrothermal growth recipes,[6,49,53,54] our ZnO nanorods were likely to have grown

along the [001] wurtzite crystal direction, with most of the catalytic surface being contributed by the less reactive non-polar (100) and (110) planes at the sides of the [001]-oriented rods. This limitation is more than overcome by the fibrous nature of the carbon cloth substrate which provides numerous surfaces for more nanorods. The end result is very high faradaic currents (*i.e.* 3 mA cm^{-2} at 1.8 V_{RHE}, shown in Fig. 5A) that significantly exceed those from ZnO nanostructures on planar surfaces, even if the ZnO had predominantly polar (001) surfaces (0.6 mA cm^{-2} at 1.8 V_{RHE}).[51]

There is also significant evidence from past reports indicating that the morphology of ZnO nanostructures plays an important role in determining the water splitting efficiency. For instance, setups employing ZnO nanotubes were found to exhibit an efficiency of ~0.45%,[4] while those using ZnO with very small nanorod diameters (<100 nm) had an efficiency of ~0.4%.[6] ZnO nanorods that were functionalized with NiO co-catalysts could also increase the efficiency to ~1.8%.[34] Therefore, with appropriate modifications to the ZnO nanorod synthesis, it may be possible to further improve the photoconversion efficiencies of the present CC-based samples.

3.2.3. Long cycling tests. Furthermore, the ZnO photoanode was found to be stable when subjected to cyclic voltammetry (CV) under constant illumination over a long duration (>1 h, 150 cycles), high voltages (0.64–2.14 V_{RHE}), and fast sweeping (100 mV s^{-1}) (Fig. 5E). The CV loops became slightly steeper over repeated cycling, probably due to charge build-up in the electric double-layer at the electrode surface. SEM imaging of the photoanode after cycling shows that the carbon fibers remained densely covered with ZnO nanorods (Fig. 5F). A closer inspection reveals that the nanorods became slightly rounded and rougher than the morphology before testing. This could be due to a small degree of photocorrosion, a process where photoexcited holes oxidize ZnO, instead of water, into oxygen gas.[55–57] In contrast, Raman spectroscopy (ESI, Fig. S3†) detected no significant difference in the samples before and after cyclic voltammetry, indicating that there was little change in the chemical structure of the electrode surface during electrolysis.

3.2.4. Electronic band diagram for the ZnO photoanode. Band diagrams for the heterostructures in the photoanodes are shown in Fig. 6. The energy levels were obtained from ultraviolet photoelectron spectroscopy (UPS) and literature sources,[12,58] with details available in the ESI (S4).† Since the valence band (VB) edge of ZnO is at a lower level than that of the OER and the bandgap of ZnO (3.26 eV) is larger than the water splitting reaction potential (1.23 eV), the photoexcited holes possess sufficient energy to oxidize H_2O into O_2 gas.[16] Given that as-grown ZnO is n-type, its conduction and valence bands tend to bend upwards towards the interface with the electrolyte,[59] which helps drive photoexcited holes towards the electrolyte for the OER and reduces the chances of them recombining with electrons prematurely. The photoexcited electrons in the conduction band (CB), on the other hand, can move towards the substrate and then to the cathode *via* the external circuit to participate in the HER.

Notably, the difference between the work functions of ZnO and the substrates (CC and ITO) resulted in a Schottky junction with a barrier height of ~0.5 eV at the ZnO/CC and ZnO/ITO interfaces. This corresponds well with our experimental data, which indicates that significant photocurrents were obtained only after a positive bias of >0.5 V was applied to the substrates (Fig. 5A and B), thus lending credence to the band diagram in Fig. 6. In addition, because the work functions of the carbon cloth and ITO substrates are so similar (~4.5 eV), the improved photoelectrochemical performance in CC-based electrodes over ITO-based electrodes is unlikely to be rooted in differences in the electronic properties of the substrate

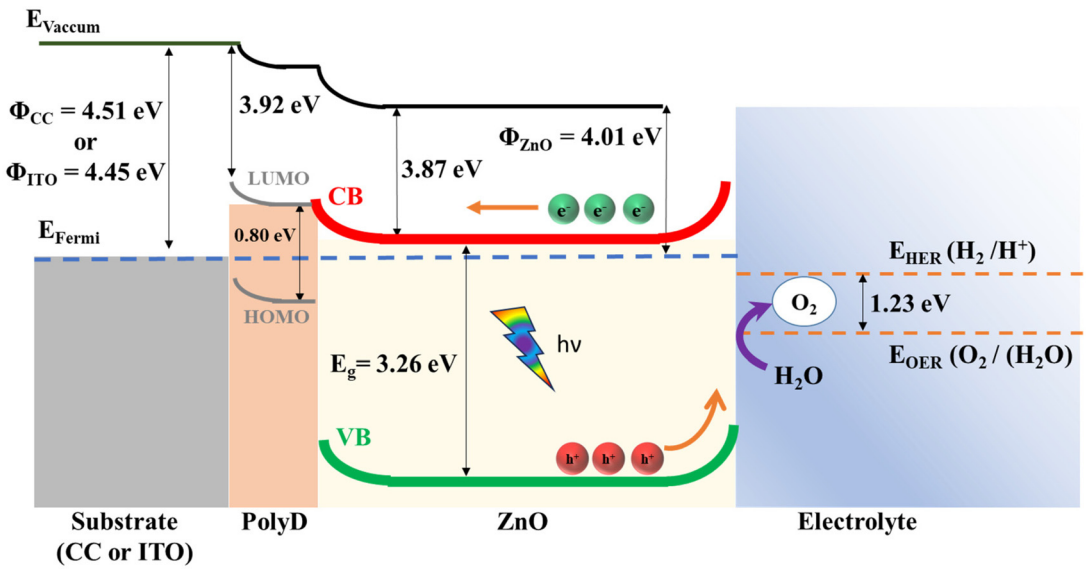

Fig. 6 Band diagram of the heterostructures in the photoanode. Further details about the energy levels can be found in the ESI (S4).†

materials. Instead, it can be attributed to an increased availability of the photocatalytic ZnO material on the fibrous carbon cloth surface, which will be confirmed in section 3.2.6.

Apart from its function as an adhesion promoter, the polydopamine layer is also useful as a charge transfer layer between ZnO and the substrates. The energy level of its lowest unoccupied molecular orbital (LUMO) is very similar to that of the conduction band edge of ZnO, enabling the photoexcited electrons in ZnO to flow easily to the substrate. Polydopamine also contains a large density of π electrons due to conjugate bonds from its numerous indole and quinone groups[58] and high carrier mobility,[13] which has been shown to be useful for charge transfer in other heterojunction catalysts.[60] Polydopamine has a small bandgap of 0.8 eV (ref. 58) which enables it to absorb light across most of the solar spectrum, whereas the large bandgap of ZnO limits it to absorption mainly in the UV region (Fig. 3C). However, due to the large barrier caused by the energy difference (~2.4 eV) between the highest occupied molecular orbital (HOMO) of polydopamine and the valence band (VB) of ZnO, it is very difficult for polydopamine's photogenerated holes to travel to the electrolyte and participate in the OER. Therefore, it is likely that the polydopamine layer has very limited functions as a photocatalyst.

3.2.5. Ni cathode. Linear sweep voltammetry (LSV) curves of fibrous (Ni/CC and CC only) and planar cathodes (Ni/Cu) are compared in Fig. 7A. While plain CC exhibited very limited catalytic activity over the range of voltages tested, Ni coated electrodes showed a distinct faradaic slope for the hydrogen evolution reaction (HER). Ni/CC, in particular, produced considerable current density even at small voltages (−0.4 V to 0 V). This is probably due to significant capacitive currents arising from the large surface area offered by the microfiber morphology of the carbon cloth.

To eliminate the influence of the capacitive current, chronoamperometric electrochemical characterization of the samples was performed (Fig. 7B).[50] The overpotential@10 mA cm^{-2} for Ni/CC was found to be 0.54 V, which is 90 mV smaller than that for Ni/Cu foil (0.63 V). At higher current densities, this difference in overpotential shrinks, as the Tafel slope of Ni/CC was 0.40 V dec^{-1}, comparatively steeper than that of Ni/Cu foil (0.32 V dec^{-1}). In fact, Fig. 7A indicates that Ni/CC would exhibit a larger overpotential than Ni/Cu for current densities greater than −55 mA cm^{-2}. The complex and non-planar surfaces in CC could have presented regions of concentrated electric fields. These can cause the HER reaction to proceed at a smaller effective potential at localized regions, resulting in an earlier onset of the faradaic slope. Conversely, there may also be regions of weaker electric fields, resulting in a smaller localized reaction rate with the faradaic slope being less steep than that of the Ni/Cu foil.

For comparison, literature reports on the HER with Ni catalysts generally report overpotentials of 0.16–0.31 V and a Tafel slope of 0.18 V dec^{-1}.[30,61,62] The relative underperformance of the present nickel electrodes may be due to the near-neutral pH (=7.5) of the electrolyte used in this study, as it has been shown that Ni electrodes exhibited negligible electrochemical activity when the electrolyte had a pH of 7.[30] In contrast, 1 M KOH was frequently used as an electrolyte in other studies.

3.2.6. Double-layer capacitance. Cyclic voltammetry (CV) with different scan rates was also performed on fibrous and planar electrodes (Fig. 8) at non-faradaic potential regions. A typical set of CV loops is presented in Fig. 8A and loops from different samples are compared in Fig. 8B. Data from the strongest current during cathodic scan are plotted against the scan rate for various electrode samples in Fig. 8C, where the slope of the data points corresponds to the double layer capacitance (C_{dl}), which is indicative of the electrochemically active surface area (ECSA).[63]

From Fig. 8C, it is observed that the capacitances of the fibrous CC-based electrodes, ZnO-nr/CC (4.4 mF cm^{-2}) and Ni/CC (3.0 mF cm^{-2}), are in line with the results of previous reports on functionalized CC,[18,21,22] and much higher than those of their planar counterparts. This directly confirms our hypothesis in the previous sections that the high linear sweep

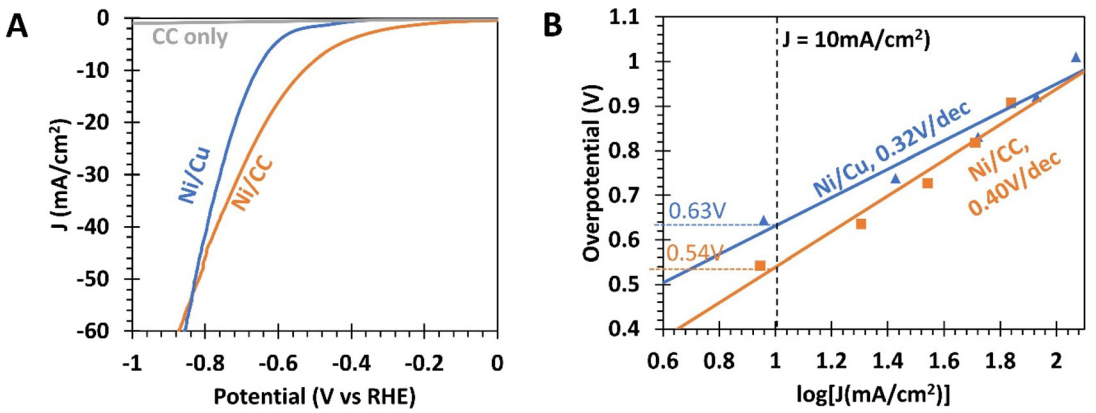

Fig. 7 (A) Linear sweep voltammetry (LSV) curves of nickel coated carbon cloth (Ni/CC), nickel coated copper foil (Ni/Cu), and carbon cloth (CC) cathodes. (B) Overpotential for the HER from various cathodes as a function of current density, obtained from chronoamperometry (CA) measurements. The data have been *iR*-compensated (see the ESI, S1†).

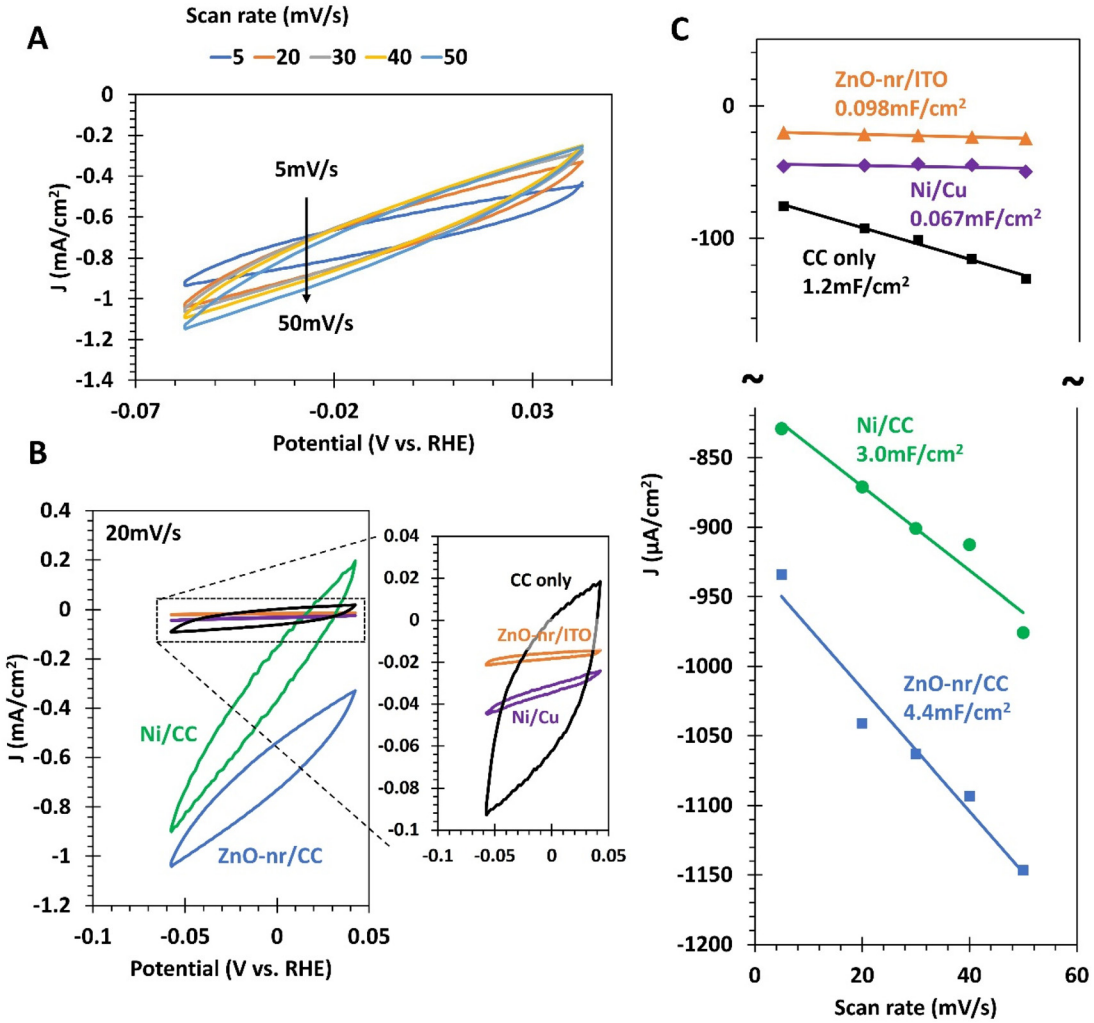

Fig. 8 (A) A series of CV loops at different scan rates taken from ZnO-nr/CC. (B) Comparison of different CV curves taken at 20 mV s^{-1} from different samples: ZnO nanorods-on-carbon cloth (ZnO-nr/CC), nanorods-on-ITO/glass (ZnO-nr/ITO), nickel-on-carbon cloth (Ni/CC), and nickel-on-copper foil (Ni/Cu) samples. (C) Current density as a function of scan rate during cyclic voltammetry (CV) from different samples. The double-layer capacitance (C_{dl}) is calculated from the magnitude of the fitted linear slope.

voltammetry currents obtained for the ZnO-nr/CC photoanode (Fig. 5A) and Ni/CC cathode (Fig. 7A), as well as the relatively slow response of ZnO-nr/CC to a change in illumination (Fig. 5C), are due to a large double layer capacitance for CC-based electrodes.

Importantly, ZnO-nr/CC had 44.9 times the capacitance of ZnO-nr/ITO, which is almost exactly the same improvement that Ni/CC had over Ni/Cu (44.8×). This result suggests that the increase in capacitance is likely due to the same source – an increase in the actual surface area due to the fibrous microstructure of CC, which significantly increased the number of electrochemical reaction sites. To further support this point, we also note that ZnO-nr/CC had 1.47× the capacitance of Ni/CC which is, again, the exact same improvement of ZnO-nr/ITO over Ni/Cu. In this case, the increase in reaction sites came from the additional surface generated by the nanorod morphology of ZnO. It is worth noting that, other than the surface area, the surface chemistry clearly mattered too, as the capacitance of plain CC was 2.5×–3.7× smaller than those of its functionalized counterparts (Fig. 8C).

The key to achieving such favorable surface chemistry on a large surface area for water splitting reactions is the use of polydopamine-assisted electroless deposition. The result of this study shows that electroless deposition has a very high throwing power *i.e.* the ability to deposit materials uniformly on geometrically complex surfaces. This enabled the growth of a uniform coating of functional Ni and ZnO on the microfibers, fully utilizing the available surface to deposit large amounts of catalytic material.

3.2.7. Overall water splitting. The overall water splitting process for different combinations of planar electrodes (ZnO-nr/ITO–Ni/Cu foil) and fibrous electrodes (ZnO-nr/CC–Ni/CC) was studied in two-electrode setups (Fig. 9). The linear sweep trends in Fig. 9A and B were observed to be highly similar to

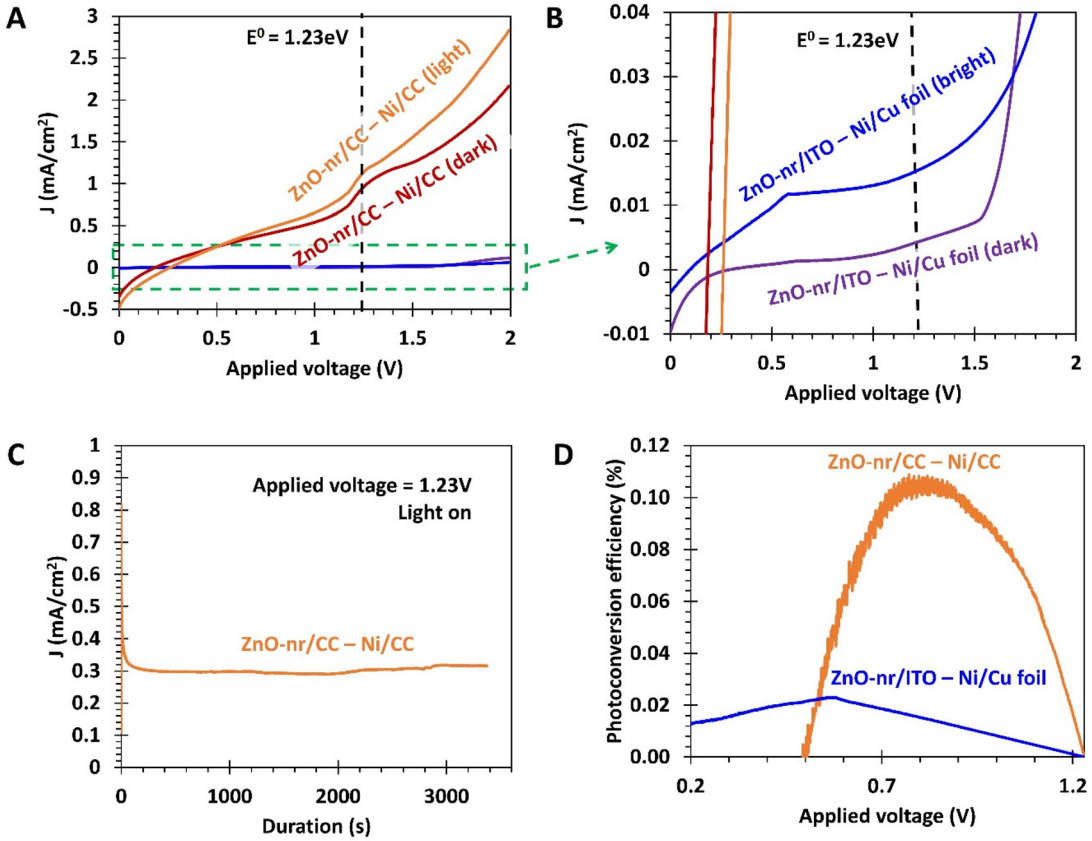

Fig. 9 (A) Linear sweep of two electrode setups with a ZnO-nr/CC anode with a Ni/CC cathode and (B) a ZnO-nr/ITO anode with a Ni/Cu cathode under AM1.5 light and dark conditions. (C) Photostability of ZnO-nr/CC (anode)–Ni/CC (cathode) under continuous illumination of AM1.5 light. (D) Photoconversion efficiency of planar and CC-based electrodes.

the OER curves (Fig. 5A and B), indicating that the overall water splitting reaction was strongly limited by the OER, regardless of the electrode morphology. Furthermore, the setup with the ZnO-nr/CC photoanode demonstrated excellent stability over extended periods of electrolysis under illumination (Fig. 9C), which is consistent with the results of cyclic tests shown in Fig. 5C.

To assess the 2-electrode photoconversion efficiency, η, of the setups, we used the earlier-mentioned eqn (5) with the voltage V term replaced with the applied potential (V_{app}) under the 2-electrode measurement setup:

$$\eta = \frac{J'(1.23 - V_{app})}{P_{in}}. \quad (6)$$

The efficiencies of the fibrous and planar electrode setups were found to reach maximum values of ~0.11% and ~0.02%, respectively (Fig. 9D), with the fibrous electrode setup offering a 5.5 times improvement. Interestingly, despite the unidirectionality of the incident light and the same apparent illumination area, the setup employing the fibrous ZnO-nr/CC photoanode was more efficient than that using the planar ZnO-nr/ITO photoanode. A possible reason for this could be that the incident light was scattered forward, further into the depths of the fibrous ZnO-nr/CC electrode, resulting in additional photoexcitation opportunities for the nanorods beneath the surface of the carbon cloth. In contrast, the incident light can only be scattered backwards without much interaction with the nanorods for the planar ZnO-nr/ITO electrode.

4. Discussion

To the best of our knowledge, this is the first study conducted for a water splitting photoanode made from fibrous carbon cloth functionalized with ZnO nanorods. By utilizing a polydopamine-assisted electroless deposition process, ZnO nanostructures and Ni film were uniformly deposited on the highly uneven microfiber surfaces of the carbon cloth, which enabled a large amount of catalytic material to participate in the water splitting reactions. This was confirmed by cyclic voltammetry measurements, which indicated an ~2 order of magnitude increase in electrochemically active surface area (ECSA) of ZnO-nr/CC electrodes compared to that of planar ZnO-nr/ITO electrodes (Fig. 8C). The enhanced surface area provided by the carbon cloth fibers for adherent ZnO nanorod growth (Fig. 2A and B) turned out to be key to a better photoelectrochemical performance (Fig. 5C), as the electronic band pro-

perties of carbon cloth were too similar to those of ITO to cause a change in the water splitting efficiency (Fig. 6).

Some advantages offered by the CC-based electrodes include smaller onset potentials for both the HER (with Ni) and the OER (with ZnO) and more than 5 times improvement in photoconversion efficiency for carbon cloth electrodes compared to that of their planar counterparts. The dark current of ZnO-nr/CC was also found to be ~40 times larger than that of planar samples, implying that ZnO-nr/CC can provide significant water splitting activity at low voltages even under ambient lighting.

Furthermore, ZnO-nr/CC photoanodes exhibited a maximum photoconversion efficiency of 0.45% in 3-electrode measurements, which was substantially higher than those of ZnO nanostructures fabricated on planar substrates reported here (0.05%) and elsewhere (0.03%–0.15%).[4,5,8,34] When paired with Ni-based cathodes in a 2-electrode setup, the maximum efficiencies were reduced to 0.11% (fibrous) and 0.02% (planar), possibly due to the overpotentials of the cathode which were excluded in 3-electrode measurements. Nevertheless, the CC-based fibrous electrodes demonstrated a significant 5.5× improvement over planar electrodes. It is also worth noting that 2-electrode efficiencies were rarely reported in previous ZnO-related water splitting studies, despite having greater practical significance and being strongly recommended by Walter *et al.*[16] over 3-electrode efficiencies.

Lastly, apart from the initial pyrolysis procedure for the production of the carbon cloth, all other synthesis processes occurred at very mild temperatures of below 100 °C. This contrasts with the conventional method of ZnO nanorod synthesis, which requires the spin-coated sol–gel to be subjected to a high temperature treatment step of ~500 °C to generate the ZnO seed layer.[11] The aqueous-based synthesis techniques reported here are also highly scalable to large substrate sizes and use relatively cost-effective chemical precursors and materials. Furthermore, the water splitting setup uses a near-neutral electrolyte (pH = 7.5), which ensures a long working life of the setup. Therefore, apart from improved performance over planar electrodes, the use of carbon cloth and polydopamine-assisted electroless deposition also offers practical advantages in the development of photoelectrochemical water splitting plants.

5. Conclusions

Electroless deposition was used to synthesize ZnO and Ni nanomaterials uniformly on highly complex surfaces of carbon cloth (CC) microfibers. Particularly, polydopamine-assisted electroless deposition was successfully demonstrated as an alternative method to deposit the seed layer of ZnO, prior to the usual hydrothermal growth of ZnO nanorods. The resultant ZnO nanorods are of good crystalline quality and demonstrate good coverage over the substrate, which is essential for achieving good photoelectrochemical performance.

The morphology of the substrate has a profound effect on the photoelectrochemical performance in water splitting. The fibrous morphology provided by carbon cloth offers a large surface for the functionalization of the catalytic material in the form of ZnO nanorods and Ni nanofilms. In ZnO nanorod photoanodes, CC substrates enable more than 5 times improvement of photoconversion efficiencies, smaller onset potentials (1.1 V_{RHE} *vs.* 1.8 V_{RHE}), and 40 times larger dark faradaic currents at 1.23 V_{RHE} compared to ZnO grown on planar ITO-based substrates. CC substrates also enable Ni cathodes to experience ~90 mV smaller overpotential@10 mA cm^{-2}, but at the expense of a larger Tafel slope. The photocurrent obtained from the ZnO-nr/CC anode is highly stable with the peak current decreasing by only ~5% across 5 cycles of illumination, compared to the ~72% decrease experienced by the planar ZnO-nr/ITO anode. However, the response of the CC-based photoanodes to changes in the illumination conditions is slower, taking hundreds of seconds to reach the peak photocurrent, compared to the tens of seconds taken by the planar electrodes. The double-layer capacitance of the electrodes was measured using cyclic voltammetry, showing that the increased efficiency of the ZnO-nr/CC anode is due to an almost 2 order of magnitude increase in electrochemically active sites. This is provided by the copious surface of the microfiber morphology in the carbon cloth.

The aqueous based material synthesis procedures presented here are easy to implement and highly amenable for scaling up over large areas. The electrochemical experiments were conducted at near neutral pH, which is helpful for sustainable and safe operation.

Author contributions

Ian P. Seetoh contributed to conceptualization, data curation, formal analysis, experimental investigations, visualization, methodology, and writing of the original draft. Akhil K. Ramesh contributed to conceptualization, methodology, experimental investigations, and writing of the original draft. Wei Xin Tan contributed to experimental investigations and writing of the original draft. Chang Quan Lai contributed to conceptualization, resources, supervision, funding acquisition, methodology, project administration, and writing (review and editing).

Conflicts of interest

The authors declare no conflicts of interest.

Acknowledgements

This work was partially supported by C. Q. L.'s Nanyang Assistant Professorship grant (award no.: 022081-00001) and MOE AcRF Tier 1 grant (award no.: RT15/22).

References

1 A. Raveendran, M. Chandran and R. Dhanusuraman, A comprehensive review on the electrochemical parameters and recent material development of electrochemical water splitting electrocatalysts, *RSC Adv.*, 2023, **13**, 3843–3876.
2 A. Krishnan, *et al.*, Ni-based Electro/Photo-Catalysts in HER – A Review, *Surf. Interfaces*, 2023, **36**, 102619.
3 Z. Cai, *et al.*, Simple and cost effective fabrication of 3D porous core–shell Ni nanochains@NiFe layered double hydroxide nanosheet bifunctional electrocatalysts for overall water splitting, *J. Mater. Chem. A*, 2019, **7**, 21722–21729.
4 W. C. Lee, *et al.*, Marangoni ring-templated vertically aligned ZnO nanotube arrays with enhanced photocatalytic hydrogen production, *Mater. Chem. Phys.*, 2015, **149–150**, 12–16.
5 A. Wolcott, W. A. Smith, T. R. Kuykendall, Y. Zhao and J. Z. Zhang, Photoelectrochemical Study of Nanostructured ZnO Thin Films for Hydrogen Generation from Water Splitting, *Adv. Funct. Mater.*, 2009, **19**, 1849–1856.
6 E. S. Babu, S.-K. Hong, T. S. Vo, J.-R. Jeong and H. K. Cho, Photoelectrochemical water splitting properties of hydrothermally-grown ZnO nanorods with controlled diameters, *Electron. Mater. Lett.*, 2015, **11**, 65–72.
7 Y. Wei, *et al.*, Polydopamine-assisted decoration of ZnO nanorods with Ag nanoparticles: an improved photoelectrochemical anode, *J. Mater. Chem. A*, 2013, **1**, 5045–5052.
8 P. Sahoo, A. Sharma, S. Padhan and R. Thangavel, Construction of ZnO@NiO heterostructure photoelectrodes for improved photoelectrochemical performance, *Int. J. Hydrogen Energy*, 2021, **46**, 36176–36188.
9 Y.-K. Hsu, Y.-C. Chen and Y.-G. Lin, *Novel ZnO/Fe2O3 Core–Shell Nanowires for Photoelectrochemical Water Splitting*, ACS Publications, 2015. DOI: **10.1021/acsami.5b03921**. **https://pubs.acs.org/doi/pdf/10.1021/acsami.5b03921**.
10 X. An and Y. Zhang, Fabrication of NiO quantum dot-modified ZnO nanorod arrays for efficient photoelectrochemical water splitting, *Appl. Phys. A*, 2017, **123**, 647.
11 Z. R. Tian, *et al.*, Complex and oriented ZnO nanostructures, *Nat. Mater.*, 2003, **2**, 821–826.
12 J. O. Hwang, *et al.*, Vertical ZnO nanowires/graphene hybrids for transparent and flexible field emission, *J. Mater. Chem.*, 2011, **21**, 3432–3437.
13 J. Kegel, I. M. Povey and M. E. Pemble, Zinc oxide for solar water splitting: A brief review of the material's challenges and associated opportunities, *Nano Energy*, 2018, **54**, 409–428.
14 L. Vayssieres, K. Keis, A. Hagfeldt and S.-E. Lindquist, Three-Dimensional Array of Highly Oriented Crystalline ZnO Microtubes, *Chem. Mater.*, 2001, **13**, 4395–4398.
15 J. Qiu, *et al.*, Morphology transformation from ZnO nanorod arrays to ZnO dense film induced by KCl in aqueous solution, *Thin Solid Films*, 2008, **517**, 626–630.
16 M. G. Walter, *et al.*, Solar Water Splitting Cells, *Chem. Rev.*, 2010, **110**, 6446–6473.
17 P. Arunachalam and A. M. Al Mayouf, Chapter 28 - Photoelectrochemical Water Splitting, in *Noble Metal-Metal Oxide Hybrid Nanoparticles*, ed. S. Mohapatra, T. A. Nguyen and P. Nguyen-Tri, Woodhead Publishing, 2019, pp. 585–606. DOI: **10.1016/B978-0-12-814134-2.00028-0**.
18 Y. Zhang, *et al.*, Ultrafine Metal Nanoparticles/N-Doped Porous Carbon Hybrids Coated on Carbon Fibers as Flexible and Binder-Free Water Splitting Catalysts, *Adv. Energy Mater.*, 2017, **7**, 1700220.
19 C. Zhang, *et al.*, Nitrogen-doped flexible carbon cloth for durable metal free electrocatalyst for overall water splitting, *Surf. Coat. Technol.*, 2018, **347**, 407–413.
20 Q. Wang, *et al.*, Design of active nickel single-atom decorated MoS2 as a pH-universal catalyst for hydrogen evolution reaction, *Nano Energy*, 2018, **53**, 458–467.
21 Z. Shen, *et al.*, An active ZnxNi1-xS@Mo2C/carbon cloth electrode as efficient catalyst for water electrolysis, *Vacuum*, 2022, **196**, 110729.
22 X.-Z. Fan, *et al.*, Intrinsic-structural-modulated carbon cloth as efficient electrocatalyst for water oxidation, *Appl. Catal., B*, 2021, **292**, 120152.
23 M. Izaki and T. Omi, Transparent Zinc Oxide Films Chemically Prepared from Aqueous Solution, *J. Electrochem. Soc.*, 1997, **144**, L3.
24 M. A. Ruíz-Gómez, *et al.*, Electroless controllable growth of ZnO films and their morphology-dependent antimicrobial properties, *J. Hazard. Mater.*, 2018, **347**, 39–47.
25 F. Song, *et al.*, Transition Metal Oxides as Electrocatalysts for the Oxygen Evolution Reaction in Alkaline Solutions: An Application-Inspired Renaissance, *J. Am. Chem. Soc.*, 2018, **140**, 7748–7759.
26 L. Huo, *et al.*, Applications of Nickel-Based Electrocatalysts for Hydrogen Evolution Reaction, *Adv. Energy Sustainability Res.*, 2022, **3**, 2100189.
27 Y. Xu, C. Wang, Y. Huang and J. Fu, Recent advances in electrocatalysts for neutral and large-current-density water electrolysis, *Nano Energy*, 2021, **80**, 105545.
28 J. Chen, *et al.*, Reversible hydrogen spillover in Ru-WO3-x enhances hydrogen evolution activity in neutral pH water splitting, *Nat. Commun.*, 2022, **13**, 5382.
29 K. Obata, R. van de Krol, M. Schwarze, R. Schomäcker and F. F. Abdi, In situ observation of pH change during water splitting in neutral pH conditions: impact of natural convection driven by buoyancy effects, *Energy Environ. Sci.*, 2020, **13**, 5104–5116.
30 L. Zeng, *et al.*, Neutral-pH overall water splitting catalyzed efficiently by a hollow and porous structured ternary nickel sulfoselenide electrocatalyst, *J. Mater. Chem. A*, 2019, **7**, 16793–16802.
31 W. Oelßner, F. Berthold and U. Guth, The iR drop – well-known but often underestimated in electrochemical polarization measurements and corrosion testing, *Mater. Corros.*, 2006, **57**, 455–466.
32 *iR*-Compensation: potentiostat fundamentals/basics of EIS Gamry instruments. **https://www.gamry.com/application-notes/instrumentation/understanding-ir-compensation/**.

33 C. Q. Lai, *et al.*, Exceptional energy absorption characteristics and compressive resilience of functional carbon foams scalably and sustainably derived from additively manufactured kraft paper, *Addit. Manuf.*, 2022, **58**, 102992.
34 Y. Mao, *et al.*, Amorphous NiO electrocatalyst overcoated ZnO nanorod photoanodes for enhanced photoelectrochemical performance, *New J. Chem.*, 2016, **40**, 107–112.
35 H. Lee, S. M. Dellatore, W. M. Miller and P. B. Messersmith, Mussel-Inspired Surface Chemistry for Multifunctional Coatings, *Science*, 2007, **318**, 426–430.
36 J. H. Ryu, P. B. Messersmith and H. Lee, Polydopamine Surface Chemistry: A Decade of Discovery, *ACS Appl. Mater. Interfaces*, 2018, **10**, 7523–7540.
37 J. Qin, *et al.*, Achieving stable Na metal cycling via polydopamine/multilayer graphene coating of a polypropylene separator, *Nat. Commun.*, 2021, **12**, 5786.
38 X. Han, L. Zhang and C. Li, Preparation of polydopamine-functionalized graphene–Fe 3 O 4 magnetic composites with high adsorption capacities, *RSC Adv.*, 2014, **4**, 30536–30541.
39 K. G. Malollari, *et al.*, Mechanical Enhancement of Bioinspired Polydopamine Nanocoatings, *ACS Appl. Mater. Interfaces*, 2019, **11**, 43599–43607.
40 R. Batul, M. Bhave, P. J. Mahon and A. Yu, Polydopamine Nanosphere with In-Situ Loaded Gentamicin and Its Antimicrobial Activity, *Molecules*, 2020, **25**, 2090.
41 H. Hemmatpour, *et al.*, New insights in polydopamine formation via surface adsorption, *Nat. Commun.*, 2023, **14**, 664.
42 R. A. Zangmeister, T. A. Morris and M. J. Tarlov, Characterization of Polydopamine Thin Films Deposited at Short Times by Autoxidation of Dopamine, *Langmuir*, 2013, **29**, 8619–8628.
43 J.-X. Ma, *et al.*, Well-dispersed graphene-polydopamine-Pd hybrid with enhanced catalytic performance, *RSC Adv.*, 2015, **5**, 97520–97527.
44 H. Peng, X. Zhang, V. Papaefthimiou, C. Pham-Huu and V. Ritleng, Pd-functionalized polydopamine-coated polyurethane foam: a readily prepared and highly reusable structured catalyst for selective alkyne semi-hydrogenation and Suzuki coupling under air, *Green Chem.*, 2023, **25**, 264–279.
45 A. Kunfi and G. London, Polydopamine: An Emerging Material in the Catalysis of Organic Transformations, *Synthesis*, 2019, 2829–2838.
46 J. Gorham, *NIST X-ray Photoelectron Spectroscopy Database - SRD 20*, National Institute of Standards and Technology, 2012. DOI: **10.18434/T4T88K**.
47 T. J. Wood, *et al.*, Electroless deposition of multi-functional zinc oxide surfaces displaying photoconductive, superhydrophobic, photowetting, and antibacterial properties, *J. Mater. Chem.*, 2012, **22**, 3859–3867.
48 J. Y. Kim, *et al.*, Low-Temperature Fabrication of Zinc Oxide Micropatterns Using Selective Electroless Deposition, *Electrochem. Solid-State Lett.*, 2005, **8**, H75.
49 L. Vayssieres, K. Keis, S.-E. Lindquist and A. Hagfeldt, Purpose-Built Anisotropic Metal Oxide Material: 3D Highly Oriented Microrod Array of ZnO, *J. Phys. Chem. B*, 2001, **105**, 3350–3352.
50 S. Anantharaj, S. Kundu and S. Noda, Worrisome Exaggeration of Activity of Electrocatalysts Destined for Steady-State Water Electrolysis by Polarization Curves from Transient Techniques, *J. Electrochem. Soc.*, 2022, **169**, 014508.
51 A. U. Pawar, C. W. Kim, M. J. Kang and Y. S. Kang, Crystal facet engineering of ZnO photoanode for the higher water splitting efficiency with proton transferable nafion film, *Nano Energy*, 2016, **20**, 156–167.
52 J. Ma, *et al.*, Synthesis of ZnO nanosheet array film with dominant {0001} facets and enhanced photoelectrochemical performance co-sensitized by CdS/CdSe, *CrystEngComm*, 2014, **16**, 2910–2916.
53 L. Vayssieres, Growth of Arrayed Nanorods and Nanowires of ZnO from Aqueous Solutions, *Adv. Mater.*, 2003, **15**, 464–466.
54 W.-Y. Wu, C.-C. Yeh and J.-M. Ting, Effects of Seed Layer Characteristics on the Synthesis of ZnO Nanowires, *J. Am. Ceram. Soc.*, 2009, **92**, 2718–2723.
55 D. Dworschak, C. Brunnhofer and M. Valtiner, Photocorrosion of ZnO Single Crystals during Electrochemical Water Splitting, *ACS Appl. Mater. Interfaces*, 2020, **12**, 51530–51536.
56 A. Tayyebi, T. Soltani, B.-K. Lee, M. Outokesh and M. Tayebi, Novel Visible Light Photocatalytic and Photoelectrochemical (PEC) Activity of Carbon-doped Zinc Oxide/Reduced Graphene Oxide: Supercritical Methanol Synthesis with Enhanced Photocorrosion Suppression, *J. Alloys Compd.*, 2017, **723**, 1001–1010.
57 A. Serrà, *et al.*, Highly active ZnO-based biomimetic fern-like microleaves for photocatalytic water decontamination using sunlight, *Appl. Catal., B*, 2019, **248**, 129–146.
58 Y. Zou, *et al.*, Regulating the absorption spectrum of polydopamine, *Sci. Adv.*, 2020, **6**, eabb4696.
59 C. Jiang, S. J. A. Moniz, A. Wang, T. Zhang and J. Tang, Photoelectrochemical devices for solar water splitting – materials and challenges, *Chem. Soc. Rev.*, 2017, **46**, 4645–4660.
60 F. Guo, *et al.*, Z-scheme heterojunction g-C3N4@PDA/BiOBr with biomimetic polydopamine as electron transfer mediators for enhanced visible-light driven degradation of sulfamethoxazole, *Chem. Eng. J.*, 2020, **386**, 124014.
61 Z. Chen, *et al.*, Porous NiFe alloys synthesized via freeze casting as bifunctional electrocatalysts for oxygen and hydrogen evolution reaction, *Int. J. Hydrogen Energy*, 2021, **46**, 37736–37745.
62 S. Gupta, *et al.*, Co–Ni–B nanocatalyst for efficient hydrogen evolution reaction in wide pH range, *Appl. Catal., B*, 2016, **192**, 126–133.
63 D. M. Morales and M. Risch, Seven steps to reliable cyclic voltammetry measurements for the determination of double layer capacitance, *JPhys Energy*, 2021, **3**, 034013.